Increasing Milling Precision for Macro-Micro-Manipulators with Disturbance Rejection Control via Visual Feedback

Christopher Schindlbeck, Alexej Janz, Christian Pape and Eduard Reithmeier

Abstract— **Industrial robotic manipulators can be augmented by a micro-positioning unit in order to increase their precision resulting in a so called macro-micro-manipulator. The micro-positioning unit is typically driven by piezoelectric actuators due to their beneficial properties. However, contact forces during interaction tasks induce deviations from the nominal path that can not be observed due to compliance, lack of sensors in the micro-positioning unit, or unknown interaction dynamics in constrained environments. In this paper, a model-free and decoupled disturbance rejection controller via visual feedback for macro-micro-manipulators is presented. An external stereoscopic vision system is employed to detect deviations from the nominal trajectory of the macro-positioning unit. We outline an image segmentation algorithm and the utilized camera calibration technique based on two-view geometry. Afterwards, the disturbance rejection controller including visual feedback for the macro-micro-manipulator is described. In order to demonstrate the 3D capability of the proposed approach, a microscopic staircase is milled. For comparison, the milling experiment is executed without and with active piezoelectric actuator including disturbance rejection in order to show the increase in precision during the milling task. Results show that the arithmetic mean roughness falls below $2\,\mu$m for the step profiles and the maximum surface height deviation is less than $\pm 10\,\mu$m for each steps.**

I. INTRODUCTION

Dual-stage actuators (DSA) combine two mechatronic systems in a serial interconnection in order to take advantage of their complimentary features. Therein, the macro system is responsible for coarse positioning while the micro system ensures a movement with high precision. Such systems usually employ piezoelectric actuators due to their (sub)nanometer level resolution, highly dynamic behavior, large blocking force, and high mechanical stiffness [1]. These actuators exhibit nonlinear characteristics such as hysteresis and creep effects when open-loop controlled [2] but closed-loop control such as PID feedback control [3] is able to cope with these effects.

Ubiquitous examples of the DSA design paradigm can be found in a large field of application such as hard disk drives [4], [5], robotic macro-micro manipulators [6], micro-nano manipulators [7], flexure-based XY stages [8], wafer scanners for lithography [9], and scanning probe microscopy [10]. Control architectures for DSA comprise a variety of approaches such as single-input single-output designs [11], sensitivity decoupling frameworks [12], decoupled approaches [4], master-slave designs [13], [14], robust multiple-input multiple-output designs [15], anti-saturation controllers [16],

and nonlinear controllers such as sliding mode [17], [18] or adaptive control [19].

During interaction tasks, contact forces induce deviations from the nominal path due to unmodelled parameters/dynamics in the primary/secondary system and unknown interaction dynamics in constrained environments with uncertain stiffness. Such contact forces are typically treated as an undesired external disturbance which in turn necessitates disturbance rejection strategies. Active disturbance rejection control designs include observer-based strategies [20], [21] or robust control strategies for repetitive motions [22], [23]. In literature, the vast majority of DSA control architectures are applied to hard disk drives and only very few works consider systems with more than two degrees of freedom (DOF) for the micro system or were the total DOF of the macro-micro-system exceeds four.

Choice of External Measurement System

Interferometers are typically used for position feedback due to their high resolution and frequency. However, the following drawbacks make them unsuitable for highly dynamic tasks with high DOF:

- Without retroreflectors, reliable orientation measurement is only possible within a small range
- Size and weight of retroreflectors scales with traversed position/orientation
- Mass-loading by retroreflectors adds inertia to the end-effector degrading dynamic response behavior crucial for disturbance rejection
- Simultaneous position and orientation measurement can only be realized with low frequency

Although commercial interferometric devices have a high frequency ($>1\,$kHz), simultaneous orientation measurement necessitates at least three points whose distance needs to be obtained sequentially severely limiting the overall pose measurement frequency. Furthermore, such systems only have a high resolution (nanometer range) in normal direction. As a consequence, a measurement device with multiple laser beams would be needed for the realization of high-frequency six DOF pose measurements. This approach leads to systems with six laser beams that are not only expensive but the attachment of six retroreflectors to the end-effector increases its inertia and thus impedes the dynamic response behavior crucial for successful disturbance rejection.

Main Contribution

The main contribution of this paper is a disturbance rejection control design including visual feedback for 3D

All authors are with the Institute of Measurement and Automatic Control, Faculty of Mechanical Engineering, Leibniz Universität Hannover, 30167 Hannover, Germany, schindlbeck@imr.uni-hannover.de

machining operations for macro-micro-manipulators. Using a decoupled and model-free approach allows the utilization of industrial robotic systems as macro system which typically have closed control architectures. The micro system is responsible for the rejection of external disturbances detected by the external vision system in order to increase the precision during tasks with high contact forces. The overall proposed system *simultaneously* aims at:

- High Number of DOF / Versatility
- Precision
- Large size of workspace / High ratio of workspace size to system size
- Cost
- (Fast) disturbance rejection

Machining Application

In this paper, a milling task is chosen as application of the aforementioned control strategy where not only high contact forces are generated but also interaction dynamics between piezoelectric actuator, tool center point (TCP), and environment are unknown. In related work, [24], [25] investigate milling with macro/micro actuation with visual feedback where the piezoactuator is mounted to a table such that macro system and piezoactuator are not mechanically coupled and a model-based master slave architecture is employed [26]. Therein, a commercial tracking system is utilized with 440 Hz but at the cost of a measurement uncertainty of 100 μm which bottlenecks the overall precision and therefore the milling accuracy can not exceed this order of magnitude. Here, we propose a camera system that can be calibrated to have an uncertainty below 1 μm which is a key factor in increasing milling precision. Furthermore, the deviation from the nominal trajectory is handled by a disturbance rejection control strategy for a serially connected macro-micro-manipulator which has a larger workspace than the aforementioned approach. In order to show the increase in precision during milling tasks, a microscopic staircase is milled without and with piezoelectric actuator for disturbance rejection which exploits the 3D disturbance rejection capabilities of the proposed control design.

The remainder of this paper is organized as follows. In Sec. II we describe our system with its individual components. Image segmentation and camera calibration of the vision system is treated in Sec. III. Next, the underlying control architecture for the robot, the micro-positioning unit, and the disturbance rejection with visual feedback is outlined in Sec. IV. Afterwards, we present the aforementioned milling experiments in Sec. V to show the efficacy of our proposed approach. Sec. VI concludes the paper with a short summary of the results and discussion.

II. SYSTEM COMPONENTS AND DESCRIPTION

A detailed description of the proposed system (see Fig. 1) and its various components is given in the following.

A. μKRoS-316 Robot

We utilize the industrial robot μKRoS-316 (see Fig. 1b) as macro-positioning unit which was manufactured by *Bodenseewerk Gerätetechnik* and distributed by *Jenoptik*. Previous fields of application involved contact-free inspection tasks, such as ultrasonic inspection of die-casting components [27] or flux leakage inspection [28]. The system has six DOF and is driven by nine motors, where three out of six joints are driven by two motors each. It was intentionally built for high-precision manipulations tasks and has (in contact-free scenarios) a repeatability of 5 μm and an accuracy of 50 μm both in the same range of high accurate robotic systems[1] [29]. In order to achieve this, the following measures were taken. Since gears lead to parasitic effects such as backlash, the μKRoS-316 omits gearboxes and instead only direct drives are used. It should be noted that this in turn leads to relatively low torques. However, for micro manipulation this factor plays a subordinated role due to only small payloads being attached to the end-effector. Furthermore, weights and counterweights are placed such that the center of mass is located along the axis of rotation for each link facilitating gravity compensation. Although the balancing mechanisms is laid out for each link individually, the gravity compensation for the entire system works in a satisfactory way. This inherently balances the system and therefore reduces the torques necessary to reach a specified position. Additionally, the incremental encoders are equipped with densely placed tick marks. For example, the first axis encoder has 18000 tick marks and in addition an interpolator produces 128 states per line of the encoder yielding an overall resolution of $16 \cdot 10^{-5}$ degrees.

B. Micro-positioning Unit

For our micro-positioning unit we choose the 3-DOF *XYZ200M* from *Cedrat Technologies* driven by piezoelectric actuators, see Fig. 1d. It weighs about 540 g with a nominal displacement of 200 μm and a (nominal) blocked-force of 118 N in each Cartesian direction with a nanoscopic resolution of 2 nm. We command the voltage input and access strain-gauge measurements via the *ADDIDATA APCI-3120* analog-to-digital converter that has a sample time of 10 μs enabling real-time control. Each actuator is furthermore preloaded by an external elliptical spring shell made of stainless steel which not only amplifies the displacement of the piezoelectric actuators by a factor of five but also protects e.g. against tensile stress.

C. Tracking and Vision System

1) 3D Marker: A lightweight 3D marker with black velvet and white ceramic balls together with a vision system is utilized to obtain pose information of the tool center point (TCP) for real-time control. Since a unique determination of a 6-DOF pose requires at least 3 non-overlapping points

---

[1]It should be noted that the robot was constructed in the late 1980's and we compare here the accuracy and repeatability with current state-of-the-art robotic systems.
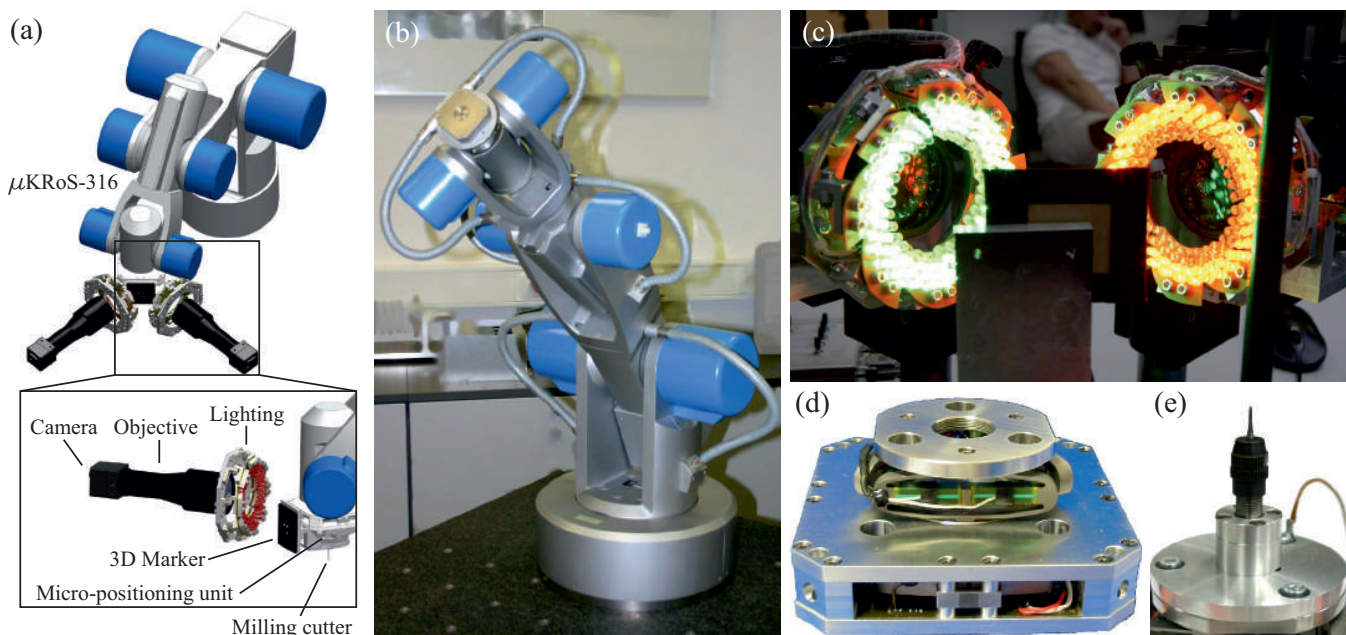
Fig. 1: Schematic of the macro-micro-manipulator setup (a) with its components: Macro-positioning unit μKRoS-316 (b), stereoscopic vision system (c), micro-positioning unit *XYZ200M* (d), and end-effector milling tool (e).

in 3D space we equip the marker with 3 white balls[2] (each with a diameter of 2.5 mm and placed in a right triangle with a leg length of 8 mm). The distance between the balls is arbitrary but constant and chosen such that it is small enough to fit into the camera images during movements and large enough to minimize image noise. To enhance contrast and therefore facilitate image processing, black velvet is used as background, see Fig. 2.

2) Cameras: For the vision system, we employ two high-speed monochrome cameras (*DALSA 1M120 Falcon*) with a resolution of 1024-by-1024 pixels and a respective pixel size of 7.4 μm. The cameras are combined with a framegrabber (*DALSA Xcelera-CL PX4 Dual*) capable of capturing 122 frames per second. Additionally, each camera is equipped with a bi-telecentric lens (*Opto Engineering TC2336*). Telecentric lenses are particularly beneficial in image processing since the change in size of projected objects is small (and therefore assumed to be negligible) under small displacements and depth of focus is increased. The lens magnification is adjusted such that together with the pixel size and camera resolution a maximum image size of 31×31 mm^2 is obtained. In order to significantly diminish the influence of external light sources and therefore facilitating image processing, red and green LED lights are placed in a circular manner around the camera objectives for illumination (see Fig. 1c).

D. Milling Tool

A brushless DC motor (*Graupner Inline400 Brushless*) with amplifier (*Maxon motor control 1-Q-EC*) weighing 62 g

[2]It should be noted that a full pose is only necessary for camera calibration purposes. Since the micro-positioning unit is a 3-DOF system, one ball would suffice for tracking control.
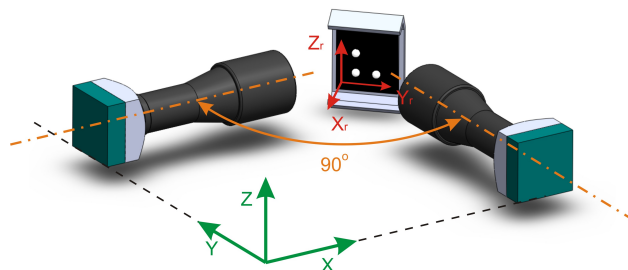

Fig. 2: Schematic for camera calibration system setup showing world frame (green) and reference frame of the 3D marker (red).

drives a milling cutter with 1415 r/min per Volt (see Fig. 1e). While a variety of milling cutters can be attached to the driving motor shaft, we will employ a milling cutter with a diameter of 1 mm in the experiments described in Sec. V. For this, the milling cutter (including electronics) is placed inside the circular opening of the piezoelectric actuator (see Fig. 1d) and attached to it via three screws.

III. IMAGE SEGMENTATION AND CAMERA CALIBRATION

Appropriate image segmentation algorithms and camera calibration of the vision system is essential before establishing a control law for the entire system. The underlying problem is the reconstruction of the 3D marker position and orientation for position control from two planar images captured by the cameras.

A. Image Segmentation

Fast image processing is crucial in order to allow real-time control. The white balls placed on the black velvet allow not only for fast, but also for precise and robust image segmentation since black velvet has favorable non-reflective properties and maximizes the contrast to the balls. White light illumination is not suited due to its broad spectrum and its respective interference effects after reflection. Therefore, red and green LEDs illuminate the 3D marker (see Fig. 1c), which guarantees light homogeneity due to their narrow spectra and the influence of the cameras onto each other is canceled out. The basic global thresholding method according to [30] is used for image segmentation:

1) Extraction of region of interest for each ball from a black and white camera image
2) Creation of a histogram and definition of initial threshold (default 125)
3) Partitioning of histogram according to (initial) threshold
4) Computation of average gray-scale values m_l and m_r of both histogram partitions
5) Computation of new (initial) threshold as mean of m_l and m_r
6) Repetition of 3), 4), and 5) until difference of old and new threshold is below a predefined tolerance

Afterwards, roundness of the identified object is analyzed via $R = (4\pi A)/C^2$, where A is the area and C the circumference. The object is treated as "successfully identified" if $R \geq 0.85$. To obtain positional information, a circle can be fitted to successfully identified objects and the corresponding equation can be brought into linear form which is then solved via least-squares regression such that the center of each fitted circle is obtained.

B. Camera Calibration

Camera calibration is needed such that real world 3D data is correctly mapped to image sensor pixels for later control purposes. Therefore, intrinsic parameters of the camera comprising focal length, skew and the principal point as well extrinsic parameters mapping world coordinates to camera coordinates have to be retrieved. These are encoded in the projection matrix $P := K \cdot [R, \boldsymbol{t}] \in \mathbb{R}^{3 \times 4}$ with calibration matrix $K \in \mathbb{R}^{3 \times 3}$, rotation matrix $R \in \mathbb{R}^{3 \times 3}$, and translational vector $\boldsymbol{t} \in \mathbb{R}^3$. K contains intrinsic and $[R, \boldsymbol{t}]$ extrinsic parameters, respectively. A point in world coordinates $\boldsymbol{W} \in \mathbb{R}^3$ is then mapped to a point in the camera image plane $\boldsymbol{w} \in \mathbb{R}^2$ via the projection matrix by $\boldsymbol{w} = P\,\boldsymbol{W}$. Since two cameras are used, stereo calibration methods can be applied here. The remainder of this section essentially follows [31]. For calibration purposes, the cameras are set up in a perpendicular configuration, see Fig. 2. Camera calibration can be carried out via the essential matrix $E \in \mathbb{R}^{3 \times 3}$ (of rank 2) which is a special case of the fundamental matrix and satisfies the epipolar constraint

$$\hat{\boldsymbol{w}}'^T E \hat{\boldsymbol{w}} = \boldsymbol{w}'^T K'^{-T} E K^{-1} \boldsymbol{w} = 0,$$

where $\hat{\boldsymbol{w}} = [x, y, z]^T$, $\hat{\boldsymbol{w}}' = [x', y', z']^T$ are the normalized image points of $\boldsymbol{w}$, $\boldsymbol{w}'$ and K, K' are calibration matrices of the two cameras, respectively. First, the calibration matrices K and K' have to be found, e.g. by straightforward calibration of each camera independently via the direct linear transformation [32]. Without loss of generality, the projection matrix of the first camera can be assumed to be $P = [\mathrm{diag}(1,1,1), \boldsymbol{0}]$, i.e. the camera coordinate system coincides with the world coordinate system. Then, the eight-point linear algorithm [33] can be used to calculate the essential matrix which consists of establishing a homogeneous linear system of equations $A \cdot \mathbf{vect}(E) = 0$, where $\mathbf{vect}$ is the vectorization operator, such that $\mathbf{vect}(E) \in \mathbb{R}^9$ concatenates the rows of the essential matrix E. The columns of A are defined as

$$\boldsymbol{a}_i = (x_i' x_i, x_i' y_i, x_i' z_i, y_i' x_i, y_i' y_i, y_i' z_i, z_i' x_i, z_i' y_i, z_i' z_i)^T$$

for N normalized image point pairs $\hat{\boldsymbol{w}}_i, \hat{\boldsymbol{w}}_i'$ with $i \in \{1, ..., N\}$. Applying ordinary least squares to the linear system yields the essential matrix. The projection matrix P' is then retrieved via subsequent singular value decomposition after projection onto the essential space $E = U \cdot \mathrm{diag}(1,1,0) \cdot V^T$ by $P'_{1/2} = [UOV^T | \pm \boldsymbol{t}]$ and $P'_{3/4} = [UO^T V^T | \pm \boldsymbol{t}]$ with $\boldsymbol{t} = U \cdot [0, 0, 1]^T$ and orthogonal matrix

$$O = \begin{bmatrix} 0 & -1 & 0 \\ 1 & 0 & 0 \\ 0 & 0 & 1 \end{bmatrix}.$$

The positive depth constraint disambiguates three physically impossible solutions (i.e. solutions that would lie behind the camera) which are subsequently discarded [34]. Finally, the Levenberg-Marquardt algorithm [35] is used to furthermore refine the projection matrices. For this, we define the reconstruction error as

$$\triangle r := \frac{1}{N} \sum_{j=1}^{N} \sqrt{(\hat{\boldsymbol{W}}_j - \boldsymbol{W}_j)^T (\hat{\boldsymbol{W}}_j - \boldsymbol{W}_j)}, \qquad (1)$$

where $\boldsymbol{W}_j$ are reference Cartesian coordinates obtained via a coordinate-measuring machine (*Werth VCIP 3D*) and $\hat{\boldsymbol{W}}_j$ are Cartesian coordinates obtained from the aforementioned approach. It should be noted that every optical system introduces a distortion of the image that needs to be considered for accurately reconstructing 3D data. However, here the camera distortion turns out to be negligible (by inspection of the reconstruction error) and instead the effect of uneven illumination is the dominating factor.

Due to slight asymmetric alignment of the LEDs, the marker is unevenly illuminated from different positions and orientations. Furthermore, due to spectral sensitivity, the camera with green LED illumination is more affected by uneven light distribution than the camera with red LED illumination. In order to improve calibration results, straight lines are fitted to each row of reference coordinates and the deviation in normal direction to coordinates from stereoscopic system are measured and stored as correction vectors in a look-up table. A trilinear interpolation of eight neighboring correction
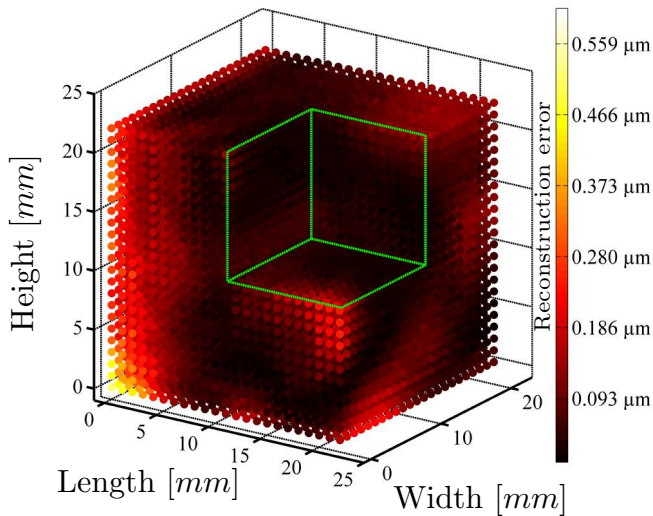
Fig. 3: Reconstruction error of calibration via essential matrix with light correction. Reference is provided by a coordinate-measuring machine.

vectors interpolates from the vectors in the look-up tables such that online position feedback is rendered possible.

Validation is done via the reconstruction error (1) and Fig. 3 depicts the final calibration results via essential matrix including light correction. The data was obtained by moving the 3D marker via the coordinate-measuring machine within a $23 \times 23 \times 23 \, \text{mm}^3$ region and simultaneously recording data with the vision system. The green cube of size $10 \times 10 \times 10 \, \text{mm}^3$ indicates a region of interest wherein the manipulation task should take place. The size was specifically chosen to enable analysis of upcoming milling experiments, see Sec. V. The average reconstruction error within the region of interest (green cube) is $0.05 \, \mu\text{m}$. A more thorough and in-depth analysis of the camera calibration process analyzing a variety of approaches can be found in [36].

IV. CONTROL DESIGN

In the following, we outline the control concept behind the disturbance rejection design for the macro-micro manipulator including the stereoscopic vision system.

A. Control of Macro- and Micro-positioning Unit

1) µKRoS-316 Robot: A commercial PID joint controller is utilized for the µKRoS-316 robot which is implemented in the industrial motion controller *UMAC* from *Delta Tau*. The controller unit is also capable of generating motion profiles such as linear trajectories which will be utilized in the milling experiments, see Sec. V. Generated trajectories are then mapped to joint profiles via inverse kinematics and then fed to the joint controller for execution.

2) Micro-positioning Unit: For the micro-positioning unit, a PID feedback controller was chosen since it exhibits more dynamic behavior than feedforward control which is crucial for fast disturbance rejection. First, system identification in the frequency domain can be established via a sweep signal.

Resonance frequencies occuring in each axis (e.g. 475 Hz for the X-axis) can be suppressed via a Notch filter [37]. Then, we fit a model with 20th order for each actuator and tune the PID parameters accordingly[3]. In order to validate the model, we obtain step response measurements with Notch filter being active. The measurement is obtained via its strain gauge sensors and is subsequently mapped to displacement after appropriate calibration. The PID parameter (e.g. $K_P = 0.3$, $K_D = 10^{-5}$, $K_I = 250$ for the X-axis) have been chosen such that a fast response time and no overshoot is possible and the control error stays within the range of $1 \, \mu\text{m}$ after $16 \, \text{ms}$. Of course, the underlying assumption is that the axis coupling is negligible which is the case for the Cartesian piezoelectric actuator used in the experiments.

B. Disturbance Rejection via Visual Feedback

When in contact with the environment, closed-loop controlled positioning devices driven by piezoelectric actuators require perturbation rejection capabilities. Here, due to lack of additional sensors in the commercial micro-positioning unit and compliant components (predominantly the spring shells), a displacement of the end-effector can not be observed when an external force acts against it. This necessitates a disturbance rejection controller which will be integrated into the macro-micro-manipulator control framework.

Let $\boldsymbol{X} \in \mathbb{R}^6$ be a 6-DOF pose comprising position and orientation of the TCP. A desired TCP pose $\boldsymbol{X}_d$ or trajectory over time is given by either a user or some high-level path planner. Through inverse kinematics a set of desired joint angles $\boldsymbol{q}_{M,d} \in \mathbb{R}^6$ for the macro robot is obtained for which the controller ensures a stable trajectory. Let $\boldsymbol{F}_{ext} \in \mathbb{R}^6$ be an unknown external wrench caused by contact with the environment during a manipulation task. This interaction causes the TCP to deviate from its nominal path resulting in $\hat{\boldsymbol{X}}$ due to unknown interaction dynamics depending on the material and its properties or compliance in the micro-positioning unit. The vision system tracks $\hat{\boldsymbol{X}}$ via the 3D marker which leads to a TCP position error $\boldsymbol{E} := \hat{\boldsymbol{X}} - \boldsymbol{X}_d$ which is compensated by the micro-positioning unit and is therefore fed as desired value expressed in its generalized coordinates $\boldsymbol{q}_{m,d} \in \mathbb{R}^3$ after an appropriate coordinate transformation. In this case, the generalized coordinates of the piezoelectric actuator are obtained by a linear coordinate transform due to being a Cartesian system. While the macro-positioning unit tracks the nominal path, the micro-positioning unit compensates external and unknown disturbances. Finally, applying the forward kinematics to the generalized coordinates of both the macro- and the micro-system yields the current TCP position $\boldsymbol{X}$. A block diagram of the proposed decoupled disturbance rejection controller design is depicted in Fig. 4.

V. EXPERIMENTS

In order to validate the disturbance rejection control approach with visual feedback, we present a milling task

---

[3]This will not be explained due to the scope of the paper and control theory literature already provides many complete studies.
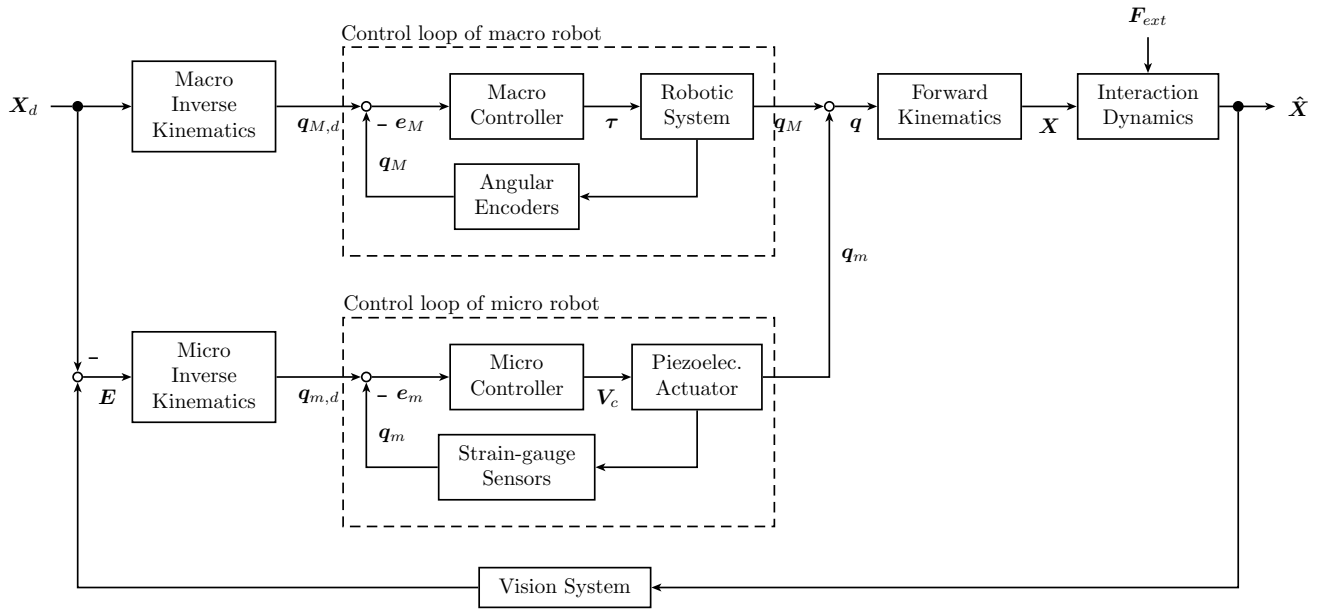
Fig. 4: Schematic block diagram of decoupled disturbance rejection design with vision feedback. External force $\boldsymbol{F}_{ext}$ and its interaction dynamics are unknown and compensated by visual feedback and micro-positioning unit. The corresponding coordinate transformations are omitted for the sake of clarity.

whose goal it is to create a microscopic staircase with the proposed system and control architecture. For comparison, the subsequent milling experiment is executed by solely using the μKRoS-316 robot and with active piezoelectric actuator for disturbance rejection. It should be noted that the presented disturbance rejection control approach can only compensate deviations from the nominal trajectory that are in the reach of the micro-positioning unit, i.e. $\pm 100\,\mu$m. Preliminary milling experiments without the micro-positioning unit showed that the induced deviations are one order of magnitude lower than the maximum displacement of the micro-positioning unit.

A. Setup for the Milling Experiment

For the experiments, an aluminum block of size $32 \times 32 \times 10\,\text{mm}^3$ with four screw holes for fixation onto a granite slab is used, see Fig. 5. On top, four cuboids of size $8 \times 8 \times 1\,\text{mm}^3$ can be used for milling. The goal is to create five steps with a step length of $300\,\mu$m and height of $50\,\mu$m each on a single cuboid. In order to get positional information of the aluminum block, a touch probe (*Renishaw TP2-5W*) is utilized which triggers at contact and retrieves the current position via the joint angles and subsequent forward kinematics. The touch probe has a repetition accuracy of $0.35\,\mu$m according to the manufacturer and we calibrate it via a spherical ruby ball with diameter of $4\,\text{mm}$ such that an average error of $10\,\mu$m is obtained. For motion planning, linear trajectories (i.e. linear in velocity) with a velocity of $0.05\,\text{mm/s}$ are generated by the industrial controller.

B. Experimental Results

Fig. 6 shows the final result for the milling experiment with piezoelectric actuator and disturbance rejection from
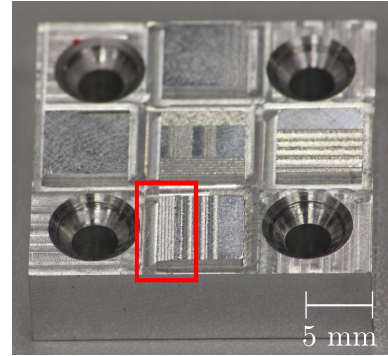

Fig. 5: Close-up view of aluminum block with holes for fixation and cuboids used for milling experiments. Area enclosed by the red box shows results of milling experiment from Sec. V-B.

three different viewpoints which were obtained via a *Keyence VK-X200* 3D confocal laser scanning microscope. An isometric viewpoint is depicted in Fig. 6a, while Fig. 6b shows five surface profiles and Fig. 6c a top view with surface details. In order to characterize the microscopic staircase, a coordinate decoupling approach can be followed which allows the usage of two independent planar characterization methods [38]. First, five step surfaces are analyzed w.r.t. their roughness and height characteristics according to ISO 4287 and ISO 25178. For this, the arithmetic mean roughness R_a of the step profiles, the maximum height of the surface S_z, and arithmetic mean surface height S_a are evaluated. Secondly, the top view can be used to extract the edge contours via edge detection, see Fig. 6c. In order to assess deviations from the nominal edge contour, a straight line is fitted to
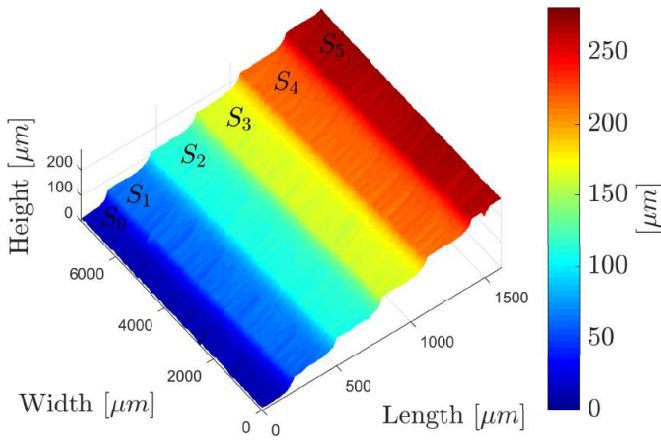
(a) 3D view of milled aluminum cuboid block.
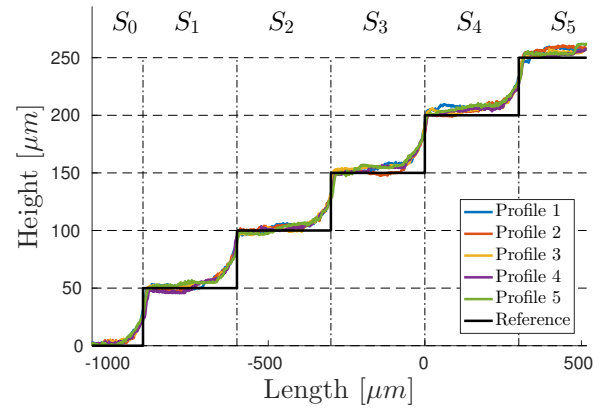
(b) Five surface profiles with reference (black line).
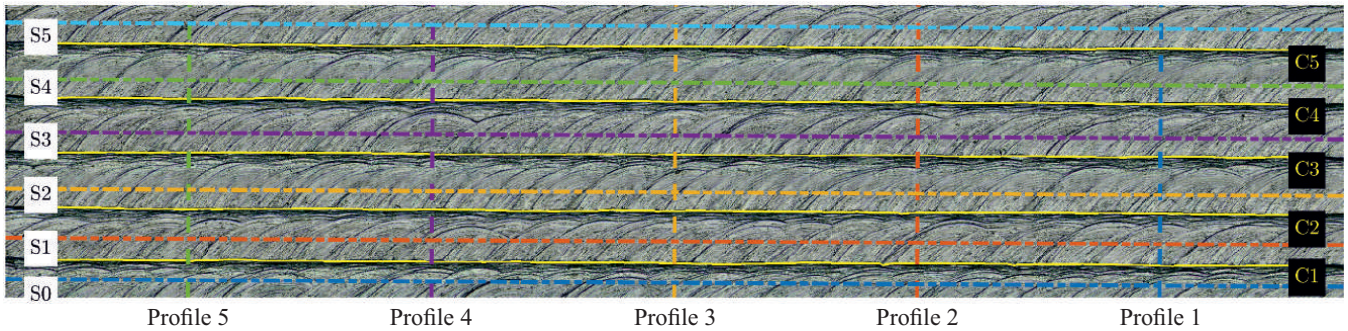
(c) Top view of milled aluminum cuboid block with steps S0-S5, edge contours C1-C5, and five surface profiles.

Fig. 6: Experimental results obtained by a confocal laser microscope showing an isometric view (a), five surface profiles (b), and the top view (c) with steps S0-S5 and edge contours C1-C5, and five surface profiles.

the data obtained from the edge detection algorithm. The aforementioned criteria and their respective values are listed in Tab. I for the experiment with and without piezoelectric actuator for disturbance rejection. The deviation from the nominal edge contour is expressed as standard and maximum deviation from the nominal line per $100\,\mu$m. An evident improvement can be observed from the experiment with active piezoelectric actuator including vision feedback in every criterion. More concretely, the arithmetic mean roughness falls below $2\,\mu$m and a maximum height of less than $20\,\mu$m, i.e. less than $\pm 10\,\mu$m in height deviation.

VI. CONCLUSION & DISCUSSION

In order to increase precision of an industrial macro-manipulator, augmentation with a micro-positioning unit and an external vision system together with a disturbance rejection control strategy was followed to compensate for external disturbances during a milling operation. For this, crucial calibration of the vision system was done via the essential matrix and additional light correction to reduce errors from external illumination by circular LEDs rings such that an average reconstruction error of $0.05\,\mu$m was obtained. For the micro-positioning unit, the PID controller and Notch filter were tuned to obtain a $1\,\mu$m tolerance band after $16\,$ms for a step response. For disturbance rejection, a decoupled design was followed whose flexibility allows

TABLE I: Quantification of results without (wo, left column) and with (w, right column) piezoelectric actuation for disturbance rejection.

Step	R_a [μm]		S_z [μm]		S_a [μm]	
	wo	w	wo	w	wo	w
S0	2.56	1.35	26.71	17.06	3.05	1.85
S1	2.60	1.60	29.61	19.62	3.33	2.10
S2	2.47	1.48	24.43	15.97	2.96	1.81
S3	2.72	1.51	27.79	16.50	3.39	1.89

Edge	Standard deviation from nominal line [μm]		Maximum deviation from nominal line [μm]	
	wo	w	wo	w
C1	2.29	1.53	9.55	6.67
C2	2.59	1.72	9.87	4.57
C3	2.79	1.69	12.34	5.82
C4	3.27	1.73	15.85	10.27

its application to commercial robotic systems with closed control architecture. A microscopic staircase was milled as a demonstrator for machining applications to evaluate the increase in precision accuracy by the proposed approach. The benefits of using a piezoelectric actuator with vision system could be observed by increased precision in the microscopic staircase utilizing standardized metrics for evaluation.

Conclusively, we have shown that the proposed disturbance rejection control strategy for the macro-micro-manipulator increases milling precision and yields more precise results than related works.

In real-world industrial manufacturing, milling processes generate dust and particles from the workpiece or milling cutter. Furthermore, a liquid coolant is often employed to cool down the cutter. Splashes from the coolant or other particles might obstruct the camera field-of-view and thus result in outliers and therefore potentially impact the disturbance rejection performance. In this work, a dry environment was chosen for the milling experiment and no effect due to occlusion of the marker due to any particles was noticed. Furthermore, any generated particles are typically orders of magnitude smaller than the balls of the marker with a diameter of 2.5 mm and since a circle fitting algorithm for the detection is used, we assume that this effect is negligible. However, in future work, any potential occlusion (e.g. due to splashes of a coolant) and its effect to the presented disturbance rejection control should be investigated more thoroughly.

REFERENCES

[1] Y. Li and Q. Xu, "Design and robust repetitive control of a new parallel-kinematic xy piezostage for micro/nanomanipulation," *IEEE/ASME Trans. Mechatron.*, vol. 17, no. 6, pp. 1120–1132, 2012.

[2] C. Schindlbeck, C. Pape, and E. Reithmeier, "Recursive online compensation of piezoelectric nonlinearities via a modified prandtl-ishlinskii approach," in *Proc. of the 20th IFAC World Congress, Toulouse*, 2017.

[3] H. Xu, T. Ono, and M. Esashi, "Precise motion control of a nanopositioning pzt microstage using integrated capacitive displacement sensors," *J. Micromech. Microeng.*, vol. 16, no. 12, pp. 2747–2754, 2006.

[4] Y.-H. Kim and S.-H. Lee, "An approach to dual-stage servo design in computer disk drives," *IEEE Trans. Contr. Syst. Technol.*, vol. 12, no. 1, pp. 12–20, 2004.

[5] K. W. Chan and W.-H. Liao, "Precision positioning of hard disk drives using piezoelectric actuators with passive damping," in *IEEE ICMA*, 2006, pp. 1269–1274.

[6] R. Li, N. D. Vuong, C.-M. Chew, and C. W. Lim, "Improving force control using zero coupling impedance criterion in series manipulator systems," *IFAC Proceedings Volumes*, vol. 46, no. 5, pp. 549–554, 2013.

[7] Y. Michellod, P. Mullhaupt, and D. Gillet, "Strategy for the control of a dual-stage nano-positioning system with a single metrology," in *IEEE ICMA*, 2006, pp. 1–8.

[8] Y. Li and Q. Xu, "Design and analysis of a totally decoupled flexure-based xy parallel micromanipulator," *Trans. Rob.*, vol. 25, no. 3, pp. 645–657, 2009.

[9] H. Butler, "Position control in lithographic equipment," *IEEE Control Syst. Mag.*, vol. 31, no. 5, pp. 28–47, 2011.

[10] T. Tuma, W. Haeberle, H. Rothuizen, J. Lygeros, A. Pantazi, and A. Sebastian, "Dual-stage nanopositioning for high-speed scanning probe microscopy," *IEEE/ASME Trans. Mechatron.*, vol. 19, no. 3, pp. 1035–1045, 2014.

[11] A. J. Fleming, "Dual-stage vertical feedback for high-speed scanning probe microscopy," *IEEE Trans. Contr. Syst. Technol.*, vol. 19, no. 1, pp. 156–165, 2011.

[12] S. Bashash, "Robust control optimization for high performance track following in hard disk drives," in *Proc. Amer. Control Conf.*, 2015, pp. 4634–4639.

[13] G. Guo, D. Wu, and T. C. Chong, "Modified dual-stage controller for dealing with secondary-stage actuator saturation," *IEEE Trans. Magn.*, vol. 39, no. 6, pp. 3587–3592, 2003.

[14] W. S. Nagel, G. M. Clayton, and K. K. Leang, "Master-slave control with hysteresis inversion for dual-stage nanopositioning systems," in *Proc. Amer. Control Conf.*, 2016, pp. 655–660.

[15] R. Nagamune, X. Huang, and R. Horowitz, "Robust control synthesis techniques for multirate and multisensing track-following servo systems in hard disk drives," *J. Dyn. Syst. Meas. Contr.*, vol. 132, no. 2, p. 021005, 2010.

[16] D. Kim, K.-T. Nam, S. H. Ji, and S. M. Lee, "Modeling of a dual actuator system and its control algorithm preventing saturation of fine actuator," in *IEEE/ASME AIM*, 2011, pp. 530–535.

[17] S.-H. Lee, "Optimal sliding mode dual-stage actuator control in computer disk drives," *J. Dyn. Syst. Meas. Contr.*, vol. 132, no. 4, p. 041003, 2010.

[18] S. Ito, J. Steininger, and G. Schitter, "Sliding mode and pid control of a dual stage actuator for precision positioning," in *IFAC Proceedings Volumes*, vol. 47, no. 3. Elsevier, 2014, pp. 6550–6555.

[19] Q. Xu and M. Jia, "Model reference adaptive control with perturbation estimation for a micropositioning system," *IEEE Trans. Contr. Syst. Technol.*, vol. 22, no. 1, pp. 352–359, 2014.

[20] H. Tang and Y. Li, "Development and active disturbance rejection control of a compliant micro-/nanopositioning piezostage with dual mode," *IEEE Trans. Ind. Electron.*, vol. 61, no. 3, pp. 1475–1492, 2014.

[21] J.-H. She, X. Xin, and Y. Pan, "Equivalent-input-disturbance approach - analysis and application to disturbance rejection in dual-stage feed drive control system," *IEEE/ASME Trans. Mechatron.*, vol. 16, no. 2, pp. 330–340, 2011.

[22] B.-S. Kim, J. Li, and T.-C. Tsao, "Two-parameter robust repetitive control with application to a novel dual-stage actuator for noncircular machining," *IEEE/ASME Trans. Mechatron.*, vol. 9, no. 4, pp. 644–652, 2004.

[23] M. Wu, B. Xu, W. Cao, and J. She, "Aperiodic disturbance rejection in repetitive-control systems," *IEEE Trans. Contr. Syst. Technol.*, vol. 22, no. 3, pp. 1044–1051, 2014.

[24] B. Olofsson, O. Sörnmo, U. Schneider, A. Robertsson, A. Puzik, and R. Johansson, "Modeling and control of a piezo-actuated high-dynamic compensation mechanism for industrial robots," in *IEEE/RSJ IROS*, 2011, pp. 4704–4709.

[25] O. Sörnmo, B. Olofsson, U. Schneider, A. Robertsson, and R. Johansson, "Increasing the milling accuracy for industrial robots using a piezo-actuated high-dynamic micro manipulator," in *IEEE/ASME AIM*, 2012, pp. 104–110.

[26] U. Schneider, B. Olofsson, O. Sörnmo, M. Drust, A. Robertsson, M. Hägele, and R. Johansson, "Integrated approach to robotic machining with macro/micro-actuation," *Rob. Comput. Integr. Manuf.*, vol. 30, no. 6, pp. 636–647, 2014.

[27] S. Hirsekorn, U. Rabe, D. Bruche, N. Grov, T. Kinzler, and W. Arnold, "Non-destructive testing of die-casting components of non-ferrous metals for surface-near porosity by high-frequency ulrasound," in *Acoustical Imaging*. Springer, 2008, pp. 223–232.

[28] Y. Li, "Development of a robot-based magnetic flux leakage inspection system," Ph.D. dissertation, Saarland University, 2011.

[29] V. Scheinman and J. M. McCarthy, *Mechanisms and Actuation*. Springer Science & Business Media, 2008, ch. Mechanisms and Actuation, pp. 67–86.

[30] R. C. Gonzalez and R. E. Woods, *Digital image processing*. Upper Saddle River: Pearson/Prentice Hall, 2008.

[31] R. Hartley and A. Zisserman, *Multiple view geometry in computer vision*, 2nd ed. Cambridge Univ. Press, 2003.

[32] Y. Abdel-Aziz, "Direct linear transformation from comparator coordinates in close-range photogrammetry," in *ASP Symp. Close-Range Photogrammetry*, 1971.

[33] H. C. Longuet-Higgins, *Readings in Computer Vision: Issues, Problems, Principles, and Paradigms*, M. A. Fischler and O. Firschein, Eds. San Francisco, CA, USA: Morgan Kaufmann Publishers Inc., 1987.

[34] Y. Ma, S. Soatto, J. Kosecka, and S. S. Sastry, *An invitation to 3-d vision: from images to geometric models*. Springer Science & Business Media, 2012, vol. 26.

[35] K. Madsen, H. B. Nielsen, and O. Tingleff, "Methods for non-linear least squares problems," 2004.

[36] A. Janz, C. Pape, and E. Reithmeier, *6D-Measurement System for the Position Determination of a Robot End-Effector*, W. Osten, Ed. Berlin, Heidelberg: Springer, 2014.

[37] S.-M. Yang and S.-C. Wang, "The detection of resonance frequency in motion control systems," *IEEE Trans. Ind. Applicat.*, vol. 50, no. 5, pp. 3423–3427, 2014.

[38] R. Leach, *Characterisation of areal surface texture*. Springer, 2013.